American Mineralogist, Volume 79, pages 411–425, 1994

Use of electron-energy loss near-edge fine structure in the study of minerals

Laurence A. J. Garvie,* Alan J. Craven
Department of Physics and Astronomy, University of Glasgow, Glasgow G12 8QQ, U.K.
Rik Brydson
Department of Materials Science and Engineering, University of Surrey, Guildford, Surrey GU2 5XH, U.K.

Abstract

High-resolution electron-energy loss near-edge fine structure (ELNES) recorded in a scanning transmission electron microscope (STEM) is shown to provide information on the local structure and bonding of specific types of atoms in minerals. The $L_{2,3}$ ELNES from Fe (Fe^{2+} and Fe^{3+}), Mn (Mn^{2+}, Mn^{3+}, and Mn^{4+}), and Cr (Cr^{3+} and Cr^{6+}) show valence-specific multiplet structures that can be used as valence fingerprints. In general, the L_3 edge for a specific 3d transition metal exhibits a chemical shift toward higher energy losses with an increase in oxidation state. Examples of mixed valence Fe- and Mn-bearing minerals are presented where the presence of multiple valence states is distinguished by a splitting of the L_3 edge. The high spatial resolution that can be obtained using the STEM allows variations in the relative proportions of the oxidation states to be detected on a scale down to 1 nm^2. This resolution is illustrated from a sample of hausmannite that shows different L_3-edge shapes consistent with variations in the Mn^{2+}-Mn^{3+} ratio over distances of ca. 100 nm. Furthermore, spectra of many elements exhibit ELNES shapes characteristic of the nearest neighbor coordination, as is demonstrated for C in the carbonate anion and Si in the SiO_4 tetrahedral unit. The C K edge from CO_3^{2-} is compared with that for elemental forms of C that exhibit very different ELNES. Similarly the Si $L_{2,3}$ ELNES from a range of SiO_4^{4-}-containing minerals all show the same near-edge shape that is very different from Si and SiC. ELNES allows for its semiquantitative analysis, which is illustrated by two theoretical techniques. Finally, the effects of electron beam damage are discussed in relation to the experimental changes observed in the ELNES.

Introduction

In a transmission electron microscope (TEM), the high-energy incident electrons that have been elastically scattered may be used to obtain images and diffraction patterns from specific regions of the sample. This allows important structural information to be deduced about the sample. The high spatial resolution offered by TEM has been useful for studying submicroscopic twins and exsolution lamellae in minerals. The TEM has also been very useful in mineralogy for high-resolution structure imaging. The incident electrons also undergo inelastic interactions with the sample (Joy, 1993) and can provide further information on the specimen. That has given rise to a number of analytical techniques, such as electron-energy loss spectroscopy (EELS), energy-dispersive X-ray spectroscopy (EDX), and Auger emission spectroscopy (AES). In EDX and AES it is the secondary processes of electron and photon emission that are studied, whereas in EELS the signal is due to the primary process of electron excitation. EELS can provide valuable information about the material under study, such as a quantitative chemical analysis on the nanometer scale. More important, the electron-energy loss near-edge structure (ELNES) of a core-loss edge can also provide information about the valency, coordination, and site symmetry of the atom undergoing excitation (e.g., Brydson et al., 1992a).

Recent advances in detector design, specifically the availability of parallel EELS (PEELS) spectrometers (Krivanek et al., 1987; Krivanek, 1989), allows data to be collected that are comparable with those obtained by X-ray absorption spectroscopy (XAS). Until recently, most EELS systems employed serial detectors with which the spectrum was acquired by scanning the signal across a single detector, one channel at a time. The development of parallel detectors, specifically multichannel arrays, has allowed a large gain in the collection efficiency, typically by a factor of 500, compared with earlier serial spectrometers. Parallel detection allows high-resolution spectra to be acquired from materials that were too beam sensitive to be collected by serial EELS at comparable spatial resolutions.

This paper demonstrates the great potential of PEELS, used in conjunction with a TEM, for providing information about the crystal chemical environment of atoms in minerals. Clay minerals and clay-sized minerals were chosen for this study, as they can be difficult to charac-

* Present address: Department of Geology, Arizona State University, Tempe, Arizona 85287-1404, U.S.A.

0003–004X/94/0506–0411$02.00

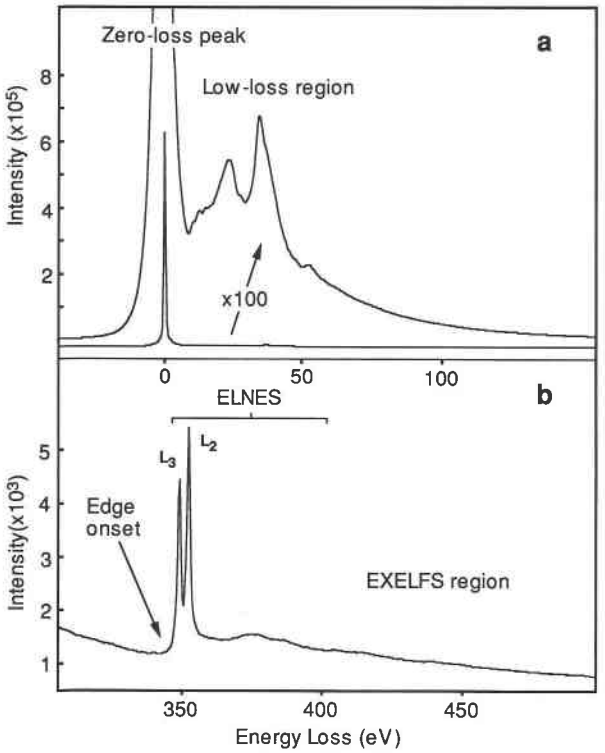

Fig. 1. A representative EELS spectrum showing (**a**) the zero-loss peak and low-loss region and (**b**) a core-loss edge from the mineral gaudefroyite. To highlight the fact that most electrons do not participate in an inelastic scattering event, the zero-loss peak is shown to scale in **a**, together with an expanded view illustrating the low-loss region. Following the low-loss region is the monitonically decreasing background. (**b**) The edge onset exhibits two intense white-line features due to the Ca $L_{2,3}$ edge. The EXELFS modulations are very weak and only just visible on the tail of the edge.

terize by conventional analytical techniques because of their fine-grained and often heterogeneous nature. The paper concentrates primarily on two types of information that can be gained from a qualitative analysis of the ELNES spectra: (1) determination of the valency of 3d transition elements, and (2) identification of local anion and cation coordinations. The ability to model ELNES is illustrated by two theoretical methods that provide semi-quantitative information on the core-loss edges and hence about the atom undergoing excitation. Consideration is also given to effects induced by the electron beam on the sample as revealed by the ELNES. Only a brief introduction to EELS is given; more detailed accounts can be found in Egerton (1986) and Buseck and Self (1992). There are many papers that deal with ELNES; introductory papers include Colliex et al. (1985), Brydson (1991), and Brydson et al. (1992a).

The EELS spectrum

An EELS spectrum (Fig. 1) displays the electron intensity as a function of energy loss and can be divided into several regions. The large zero-loss peak (ZLP) results from transmitted electrons that have undergone elastic and quasi-elastic (mainly phonon) interactions, i.e., electrons that have lost no, or very little, energy. Its width depends primarily on the energy spread and stability of the electron gun and determines the best resolution that can be obtained at the core-loss edges. The region immediately following the ZLP and extending to energy losses of ca. 50 eV, called the low-loss region, is an area of the spectrum dominated by plasmons. Plasmons can be described as resulting from the collective excitations of valence electrons. They can provide information about the dielectric function (Buechner, 1975), valence electron densities, and, in suitable cases, the phases present in alloys. Within the low-loss region are also found edges caused by transitions from outer shell electrons. Extending beyond the low-loss region in a spectrum from a thin sample is a monotonically decreasing background, arising predominantly from plasmon and single electron excitations, on which are superimposed the core-loss edges. These features result from the transition of core electrons to unoccupied states in the conduction band; this requires the energy transfer between the incident and a core electron to be greater than its binding energy. The core-loss edges usually take the form of a step, characterized by a sudden increase in intensity (Fig. 1b) that decreases in intensity with increasing energy loss. This sudden rise in intensity represents the ionization threshold, the energy of which approximately corresponds to the inner-shell binding energy and hence is characteristic of the element. Close to the thresholds and for small scattering vectors, these core-loss edge transitions are governed by the atomic dipole selection rules for the electronic transitions $\Delta l = \pm 1$, and $\Delta j = 0, \pm 1$, where l and j are the orbital and total angular momentum quantum numbers of the subshell from which the electron has been excited. The edges are classified according to the standard spectroscopic notation, e.g., the Ca $L_{2,3}$ edges in Figure 1b arise from transitions from the 2p core level.

In the first instance EELS can be used for elemental analysis, since the edges occur at energy losses equivalent to the binding energies of the core electrons in the sample, and the integrated intensity under the edge is related to the number of atoms under the electron beam. Unlike EDX, EELS can provide elemental data on all the light elements except H and He, although the latter has been detected under certain circumstances, e.g., in nanometer-sized He bubbles in irradiated Ni alloys (McGibbon, 1991).

Core-loss edges can be divided into two regions (Fig. 1b), the ELNES, extending 30–50 eV above the edge onset, and the weaker extended electron-energy loss fine structure (EXELFS). The equivalent XAS terms are XANES (X-ray absorption near-edge structure) and EXAFS (extended X-ray absorption fine structure). In a solid, the core wave functions show very little change as compared with an isolated atom. This is not the case for the outer bonding and antibonding orbitals that can in-

TABLE 1. Name, simplified formula, valence, coordination, and source of the 3d transition metal containing minerals

Mineral name	Simplified formula*	Valence and coordination	Source
	Fe-bearing minerals		
Chromite	$(Fe,Mg)(Cr,Al,Fe)_2O_4$	$^{[4]}Fe^{2+}$	Gebe Island, Indonesia
Siderite	$(Fe,Mn)CO_3$	$^{[6]}Fe^{2+}$	Ivigtut, Greenland
Hematite	Fe_2O_3	$^{[6]}Fe^{3+}$	Långban, Sweden
Iron analogue of leucite**	$KFeSi_2O_6$	$^{[4]}Fe^{3+}$	—
Chlorite (var. daphnite)	$(Fe^{2+},Al)_{12}(Si,Al)_8O_{20}(OH)_{16}\cdot nH_2O$	$^{[6]}Fe^{2+}$	Redruth, Cornwall, England
Cronstedtite	$(Fe^{2+},Fe^{3+})_6(Si,Al,Fe)_4O_{10}(OH)_8\cdot nH_2O$	$^{[6]}Fe^{2+}$, $^{[6]}Fe^{3+}$, $^{[4]}Fe^{3+}$	Wheal Jane, Cornwall, England
Nontronite	$Ca_{0.95}Fe_4(Si,Al)_8O_{20}(OH)_4\cdot nH_2O$	$^{[6]}Fe^{3+}$	Lajitas, Texas
	Mn-bearing minerals		
Ramsdellite	MnO_2	$^{[6]}Mn^{4+}$	Pirika Mine, Hokkaido, Japan
Asbolan	$Mn(O,OH)_2(Co,Ni)_x(OH)_{2x}\cdot nH_2O$	$^{[6]}Mn^{4+}$	Gebe Island, Indonesia
Norrishite	$KLiMn_4Si_8O_{24}$	$^{[6]}Mn^{3+}$	Hoskins Mine, N.S.W., Australia
Bixbyite	$(Mn,Fe)_2O_3$	$2\times{}^{[6]}Mn^{3+}$	Thomas Mt., Utah
Ganophyllite	$(K,Ca,Na)_2(Fe,Mn)_8(Si,Al)_{12}O_{29}(OH)_7\cdot nH_2O$	$^{[6]}Mn^{2+}$	Långban, Sweden
Manganosite	MnO	$^{[6]}Mn^{2+}$	Nordmark, Sweden
Hausmannite	α-Mn_3O_4	$^{[4]}Mn^{2+}$, $^{[6]}Mn^{3+}$	Kalahari Mine Field, S. Africa
	Cr-bearing minerals		
Crocoite	$PbCrO_4$	$^{[6]}Cr^{6+}$	Redlead Mine, Dundas, Tasmania
Volkonskoite	$Ca_{1.1}(Cr,Fe,Mg)_4(Si,Al)_8O_{20}(OH)_4\cdot nH_2O$	$^{[6]}Cr^{3+}$	Glazov Region, Udmurtian
Chromite	$(Fe,Mg)(Cr,Al,Fe)_2O_4$	$^{[6]}Cr^{3+}$	Gebe Island, Indonesia

* Major elements based on qualitative EDX analysis.
** Synthetic Fe analogue of leucite.

teract to form bands of orbitals that are governed by the solid-state character of the specimen and can be appreciably modified by chemical bonding. The ELNES directly probes the unoccupied orbitals and therefore reflects the environment surrounding the excited atom and can provide information on bonding, valency, coordination, and site symmetry. Note that when discussing microanalysis the edge is taken to mean all transitions from a given initial state, whereas in discussions of ELNES or XANES, the edge is taken to mean the structure in the region close to the threshold.

The EXELFS oscillations are very weak modulations of the intensity extending several hundred electron volts above the ELNES region. These oscillations are caused by an ejected electron with a low kinetic energy behaving similarly to a free electron. The ejected electron is backscattered by the surrounding atom shells, which can provide information on the coordination number and nearest neighbor distances. EXAFS studies most commonly involve analysis of K-edge modulations, such as those from the transition elements. These K-edges occur at energy losses of several thousand electron volts, where individual edges are well separated in energy. Unlike its sister technique EXAFS, EXELFS is unlikely to be widely used, since the fine structure modulations often overlap with other edges in the energy range used to collect EELS edges, typically <1000 eV.

EXPERIMENTAL SETUP

The instrument used was a VG HB5 STEM operating at 100 kV and equipped with a cold field emission gun (FEG). With this microscope, a probe size of ca. 1-nm diameter was scanned over the sample. The microscope was operated with a probe semiangle of 11 mrad, a collection angle of 12.5 mrad, and a probe current of ca. 0.5 nA. The small collection semiangle, β, ensures that the experiment is in the dipole regime for electronic transitions. A Gatan 666 parallel electron-energy loss spectrometer (PEELS) is attached to the top of the microscope column (Krivanek et al., 1987; Krivanek, 1989). To exemplify the advantage of parallel detection, an 8-s acquisition on the PEELS would require just over 1 h on a serial detection system. As well as requiring patience from the operator, long counting times have other associated problems, including C contamination, lack of microscope stability, and beam damage to the sample. The spectrometer was calibrated against the Ni L_3 edge in NiO that has a peak maximum at 853.2 eV, as determined using synchrotron radiation studies (van der Laan et al., 1986).

The samples used in this study have come from a variety of sources or were collected by one of us (L.G.) and identified by powder X-ray diffraction and EDX. The minerals containing the 3d transition metal elements are listed in Table 1, together with their formulae, selected crystallographic data, and sources. Table 2 lists minerals used in the coordination fingerprint study. Materials studied were either checked prior to study in the HB5 STEM by EDX in an SEM, or checked qualitatively by EDX in the HB5 STEM. Crystalline samples were prepared by crushing selected mineral grains in acetone and allowing a drop of the fine-grained material in suspension to dry on a lacy C-coated Cu TEM grid. Alternatively, clay samples were prepared by dispersing a small amount of material in distilled H_2O, and a small drop of the <2-μm clay fraction in suspension was dried on the above grids. Lacy C films were used so that data could be recorded from thin electron-beam transparent grains projecting over the holes. Core-loss edges were recorded with a dispersion of 0.1 or 0.05 eV per channel in order to record the detailed fine structure of the edges. The actual energy resolution is limited by the energy spread of the FEG, which is close to 0.27 eV at low probe currents. At

TABLE 2. Name, simplified formula, and source of C- and Si-containing minerals

Mineral name	Simplified formula*	Source
	C-containing minerals	
Calcite	$CaCO_3$	Llanelwedd Quarry, Wales
Siderite	$(Fe,Mn)CO_3$	Ivigtut, Greenland
Desautelsite**	$Mg_6Mn_2(CO_3)(OH)_{16}\cdot 4H_2O$	—
Hydrotalcite	$Mg_6Al_2(CO_3)(OH)_{16}\cdot 4H_2O$	Snarum, Norway
Amorphous C**	C	—
Graphite	C	South Western Graphite Mine, Texas
Diamond	C	South Africa
	Si-containing minerals	
Quartz	α-SiO_2	Llanelwedd Quarry, Wales
Talc	$(Mg,Fe)_6(Si,Al)_8O_{20}(OH)_4\cdot nH_2O$	Llanelwedd Quarry, Wales
Nontronite	$Ca_{0.95}Fe_4(Si,Al)_8O_{20}(OH)_4\cdot nH_2O$	Lajitas, Texas
β silicon carbide**	SiC	—
Si**	Si	—

* Major elements based on qualitative EDX analysis.
** Synthetic material.

normal operating currents, the width increases to a minimum of ca. 0.3 eV, which is further increased to ca. 0.45 eV by residual interference. The EELS data were typically obtained with a scanned raster from areas in the range 130 × 100 to 13 × 10 nm, with acquisition times ranging from 0.5 to 8 s. With a sample thickness of 20 nm and an irradiated area of 13 × 10 nm^2, this corresponds to a volume of roughly 2600 nm^3 and an approximate mass of 8 × 10^{-18} g (with ρ = 3 g/cm^3). Since the analyzed volume is so small, the area probed is almost invariably part of a single crystal. In a typical EELS experiment, the dose given at the sample varies from 1.25 × 10^5 e/Å^2 for a 0.5-s to 2 × 10^6 e/Å^2 for an 8-s integration time. The choice of magnification and acquisition time is governed by the stability of the material under the electron beam. For each core-loss edge recorded, three additional spectra were collected: the dark current for the core-loss edge, the low-loss region, and its corresponding dark current. The dark current arises from thermally excited current in the detector. The dark current is then subtracted from the corresponding spectrum. Before presenting the core-loss edges, a background of the form AE^{-r} was subtracted from beneath the edge, and the effect of multiple scattering and asymmetry of the ZLP were deconvoluted from the edge. The adjustable parameters A and r can be deduced by least-squares fitting of the intensity of a specific region directly preceding the core-loss edges. The topics of background subtraction and ZLP deconvolution are described in detail in Egerton (1986).

Sample thickness is an important factor when collecting EELS spectra. In order to reduce the effect of multiple scattering the thickness should be <50–100 nm for 100-kV incident electrons (Egerton, 1986). If this condition is not met, then there is an increased probability that the transmitted electron will be involved in more than one inelastic scattering event. Although the effect of a small amount of multiple scattering can be removed using deconvolution techniques, it becomes rapidly more difficult to detect edges as the specimen thickness increases. In the samples studied, abundant thin areas could always be produced by simply crushing the material in a mortar and pestle. The phyllosilicates are ideal materials for EELS study because of their platy nature, which provides abundant electron-beam transparent areas.

ELNES

Valency determination of 3d transition metals

All of the 3d transition metals are found in natural phyllosilicates, and they can be a major chemical component. Examples include roscoelite (V^{3+}), volkonskoite (Cr^{3+}), glauconite (Fe^{3+}), pennantite (Mn^{2+}), and pimelite (Ni^{2+}). Fe is by far the most common 3d transition metal in minerals. Many spectroscopic techniques have been used to determine both the oxidation state and coordination of 3d transition metals in minerals: ^{57}Fe Mössbauer spectroscopy (Cardile and Brown, 1988; Hawthorne, 1988), optical spectroscopy (Rossman, 1988), XANES (van der Laan et al., 1992; Manceau et al., 1992; Cressey et al., 1993), electron paramagnetic resonance (Calas, 1988), photoelectron spectroscopy (Rao et al., 1979), and high-resolution X-ray emission spectroscopy (Koster and Mendel, 1970; Wood and Urch, 1976). Analysis of *K*-edge XANES has proved useful in determining the coordination and oxidation state of selected transition metals in minerals (Calas and Petiau, 1983; Manceau et al., 1992). The feature that most reflects the crystal chemical environment of the transition elements is a preedge feature before the main *K* absorption edge. This has been interpreted as arising from predominantly dipole-forbidden 1s → 3d transitions and so is fairly weak in intensity. In contrast, the dipole-allowed transitions that give rise to the $L_{2,3}$ edges exhibit numerous strong sharp features or multiplet structure. Fine structure is not readily observable on the *K*-edge prepeak because of the greater core-hole lifetime broadening associated with the *K* edge than with the $L_{2,3}$ edges. The broadening on the $L_{2,3}$ edges of the 3d transition elements is typically 0.1–0.3 eV, whereas it is three to four times larger on the corresponding *K* edge. The use of PEELS to determine the oxidation

state and, in certain circumstances, the coordination of transition elements is illustrated using the $L_{2,3}$ edges from Fe, Mn, and Cr.

Several ELNES and XANES studies have shown that the $L_{2,3}$ edges from the 3d transition elements exhibit structures that are sensitive to the valence state of the metal (Otten et al., 1985; Otten and Buseck, 1987; Rask et al., 1987; Krivanek and Paterson, 1990; Paterson and Krivanek, 1990; van der Laan et al., 1992; de Groot et al., 1993; Garvie and Craven, 1993, 1994). The ELNES of the 3d transition metal $L_{2,3}$ edges are characterized by two white-line features (so called because they were first identified as such on photographic plates) that are narrow, intense peaks. These white lines arise from quasi-atomic dipole-allowed transitions from an initial state, $2p^6 3d^n$, to final states of the form $2p^5 3d^{n+1}$. The high intensity of the 3d transition metal $L_{2,3}$ edges is due to the high density of unoccupied 3d states. The two separate edges, L_3 and L_2, arise from the two ways that the spin quantum number, s, can couple to the orbital angular momentum, l, giving the total angular momentum, $j = l + s$. That gives two separate peaks due to transitions from $2p_{3/2}$ ($j = 3/2$), forming the L_3 edge, and $2p_{1/2}$ ($j = 1/2$), forming the L_2 edge. Final states of s character are also dipole allowed, but they are less intense because the dipole-allowed $2p \rightarrow s$ transitions are approximately an order of magnitude less intense than $2p \rightarrow d$ transitions. This, coupled with the fact that s and p densities of state are rather broad compared with d states, implies that the $L_{2,3}$ edges essentially represent transitions to the vacant 3d orbitals. Hence the ELNES reflects the local environment and charge state of the 3d transition metal ion in question.

An isolated 3d transition metal ion such as Mn^{2+} has five degenerate 3d orbitals. In a solid, the effect of the field from the surrounding ligands is to split the 3d orbitals into two or more separate orbitals. In minerals, the 3d transition metals are predominantly octahedrally coordinated and exhibit a wide range of symmetries. For high-spin compounds the effect of the ligands is to split the degenerate 3d orbitals into the lower energy t_{2g} and higher energy e_g orbitals. The energy difference between these two sets of orbitals is defined as the crystal field parameter, designated as 10Dq (or Δ in some texts). As will be seen later, the crystal field can have large effects on the shape of the $L_{2,3}$ edges. In the following sections on the $L_{2,3}$ edges, the discussions will be primarily concerned with the analysis of the L_3 edges, which are more intense and exhibit more multiplet structure than the broader L_2 edges. The increased broadening of the L_2 edge, in comparison with the L_3 edge, is due to the availability of the extra Coster-Kronig Auger decay channel, which reduces the lifetime of the final state and hence increases the width of the L_2 multiplet lines.

Fe. Fe is found as both Fe^{2+} and Fe^{3+} in minerals, and it is often the case that more than one valency and coordination is present in the same mineral. Minerals containing Fe^{2+} and Fe^{3+} are most commonly octahedrally coordinated, although Fe in tetrahedral coordination is sometimes found. Fe in minerals is expected to be in the high-spin state, as only strong field ligands such as CN^- can cause spin pairing. Before the discussion of the Fe $L_{2,3}$ edges for several phyllosilicates, the Fe $L_{2,3}$ edges from a number of reference minerals containing Fe^{2+} and Fe^{3+} in both octahedral and tetrahedral coordination are discussed. They are chromite ($^{[4]}Fe^{2+}$), siderite ($^{[6]}Fe^{2+}$), hematite ($^{[6]}Fe^{3+}$), and the Fe analogue of leucite ($^{[4]}Fe^{3+}$).

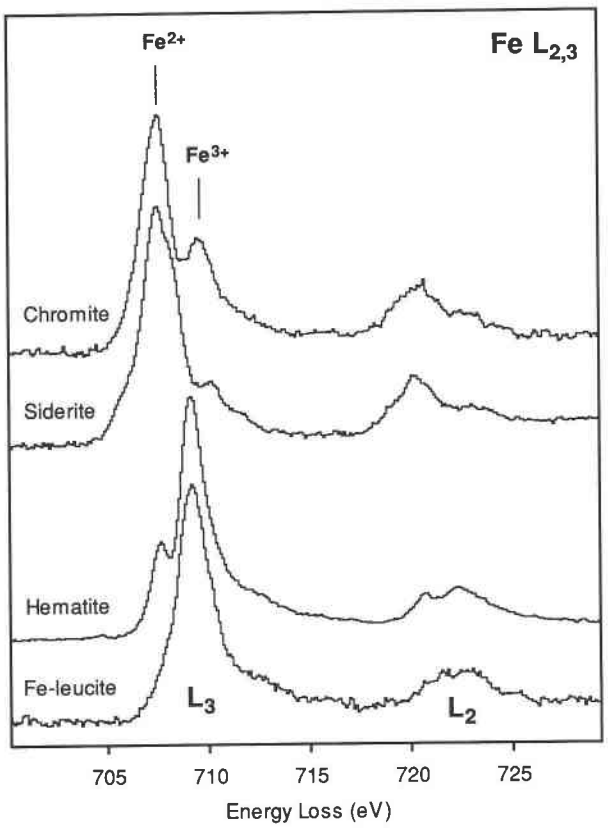

Fig. 2. Fe $L_{2,3}$ edges from reference materials. Synthetic iron analogue of leucite ($^{[4]}Fe^{3+}$), hematite ($^{[6]}Fe^{3+}$), siderite ($^{[6]}Fe^{2+}$), and chromite ($^{[4]}Fe^{2+}$). The spectra illustrated here and in subsequent figures are shown on an arbitrary scale.

The $L_{2,3}$ edges from the reference compounds (Fig. 2) all show different edge shapes, as well as a distinct chemical shift between the divalent and trivalent Fe L_3 edges (Table 3). These basic edge shapes are consistent with published Fe L_3 XANES (Cressey et al., 1993) and ELNES (Krishnan, 1990; Kurata et al., 1990) spectra. The L_3 edges for the divalent Fe minerals are at ca. 707.8 eV, and the trivalent Fe L_3 edge is 1.7 eV higher, at ca. 709.5 eV. The separation of the L_3 and L_2 peak maxima, due to spin orbit splitting, is ca. 11 eV. The Fe L_3 edges from the reference compounds illustrate that different site symmetries are recognizable by changes in the multiplet structures on the L_3 edges. Hematite has a distinctive L_3-edge shape, with a prepeak leading the main L_3 peak, whereas the Fe analogue of leucite, which contains $^{[4]}Fe^{3+}$,

TABLE 3. Energies (eV) of the L_3 and L_2 edge peak maximum for selected 3d transition metal-containing minerals

Mineral name	Element valence and coordination	L_3 peak max.	L_2 peak max.
Siderite	$^{[6]}Fe^{2+}$	707.8	720.4
Hematite	$^{[6]}Fe^{3+}$	709.5	722.6
Manganosite	$^{[6]}Mn^{2+}$	640.2	650.3
Norrishite	$^{[6]}Mn^{3+}$	642.5	653.6
Bixbyite	$^{[6]}Mn^{3+}$	641.8	652.6
Asbolan	$^{[6]}Mn^{4+}$	643.8	654.3
Chromite	$^{[6]}Cr^{3+}$	578.6	586.6
Crocoite	$^{[4]}Cr^{6+}$	580.9	589.5

Note: error in energy values is ±0.2 eV.

shows an L_3 edge without any pronounced fine structure. The $^{[6]}Fe^{2+}$ L_3 edge from siderite shows several partially resolved multiplets on both the low- and high-energy sides of the L_3 peak maximum, whereas these are not present on the L_3 edge of chromite. However, the peak at ca. 710 eV is much stronger in chromite than in siderite. The L_3 edges from hematite, the Fe analogue of leucite, and siderite correspond closely with the theoretical atomic multiplet spectra calculated by van der Laan and Kirkman (1992), which confirms the single valence and site symmetry of the Fe in these samples. However, for chromite the experimental edge has a much larger subsidiary peak at ca. 710 eV than the calculated edge for $^{[4]}Fe^{2+}$ with the appropriate 10Dq. This subsidiary peak is at approximately the correct energy for the L_3 edge from Fe^{3+}. It therefore appears that the chromite contains several percent of Fe^{3+} substituting for $^{[6]}Cr^{3+}$, as is often the case for chromite (e.g., Yang and Seccombe, 1993). The presence of Fe^{3+} in octahedral sites was confirmed by EDX, which showed that the majority of octahedral sites are filled with Cr and Al, with approximately one out of every 16 octahedral sites occupied by Fe.

The two peaks on the L_3 edge in hematite are separated by 1.5 eV, as they are in many other minerals containing $^{[6]}Fe^{3+}$ (unpublished results). These two peaks have been interpreted in terms of a simple crystal field model (Krishnan, 1990), where they have been assigned to the t_{2g} and e_g orbitals. Although such a simplistic ligand field approach appears to explain the features on the Fe L_3 edge, as well as on the Mn L_3 edges from minerals containing Mn^{3+} and Mn^{4+} (Garvie and Craven, 1993) and compounds with the valence of the 3d transition metal in the d^0 state (Brydson et al., 1987, 1989a), that is not generally the case (de Groot et al., 1990a, 1990b). The value of the crystal field strength for hematite can be estimated by comparing its L_3 edge with the calculated atomic multiplet spectra of van der Laan and Kirkman (1992). Their best fit to the experimental hematite L_3 edge is to the spectrum calculated for O_h symmetry with a 10Dq value of 2 eV, which is close to the value of 1.9 eV determined by optical spectroscopy for hematite (Marusak et al., 1980). Similarly, the values of the 10Dq can be estimated to be 1 and 0.5–1 eV for the Fe analogue of leucite and siderite, respectively.

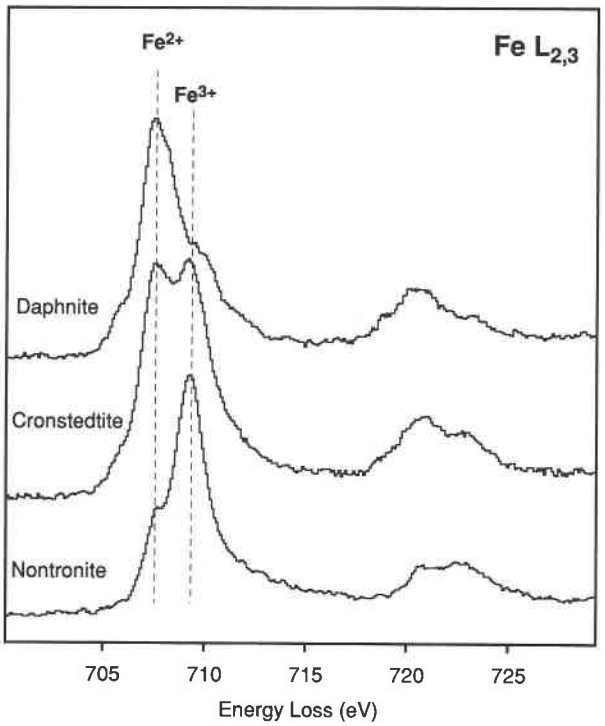

Fig. 3. Fe $L_{2,3}$ edges from three phyllosilicates. Nontronite (dominantly $^{[6]}Fe^{3+}$), cronstedtite (three distinct Fe sites, $^{[6]}Fe^{2+}$, $^{[6]}Fe^{3+}$, and $^{[4]}Fe^{3+}$) and the chlorite daphnite (dominantly $^{[6]}Fe^{2+}$ with a few percent $^{[6]}Fe^{3+}$).

The Fe $L_{2,3}$ edges from a number of phyllosilicates containing various Fe^{3+}-Fe^{2+} ratios were collected, and representative spectra are illustrated in Figure 3. The data were collected from individual well-defined clay particles, typically from areas measuring 130 × 100 nm^2. Daphnite has an Fe $L_{2,3}$ edge shape similar to that from siderite, confirming both that the Fe is octahedrally coordinated and divalent. The higher intensity of the partially resolved peak on the high-energy side of the L_3 edge, in comparison with that on the siderite L_3 edge, may indicate the presence of a small amount of Fe^{3+}. That has been confirmed for this sample by ^{57}Fe Mössbauer spectroscopy (Goodman and Bain, 1979). Cronstedtite contains a number of Fe sites: $^{[4]}Fe^{3+}$, $^{[6]}Fe^{3+}$, and $^{[6]}Fe^{2+}$ (Bailey, 1988). The presence of both Fe^{3+} and Fe^{2+} is visible from the double-peaked L_3 edge, the two edges being separated by 1.7 eV. The partially resolved peak on the low-energy side of the Fe^{2+} L_3 edge indicates that it is dominantly octahedrally coordinated, as expected from the crystal structure. Although the presence of Fe^{3+} is confirmed by the peak 1.7 eV higher in energy than the Fe^{2+} edge, it is not obvious from the L_3 edge that both $^{[6]}Fe^{3+}$ and $^{[4]}Fe^{3+}$ are present. Nontronite gives an Fe $L_{2,3}$-edge shape identical to that from hematite, indicating that the majority of the Fe is $^{[6]}Fe^{3+}$, as expected for nontronite (Güven, 1988). The splitting between the two peaks on the L_3 edge in nontronite is slightly less than in hematite, indicating a slightly smaller crystal field value.

This is consistent with the 10Dq of 1.77 eV for nontronite determined by optical spectroscopy (Bonnin et al., 1985). As illustrated by comparing the L_3 edge from hematite with that from nontronite, it is possible to obtain a relative, and possibly quantitative, measure of the crystal field strength acting on the metal ion from the multiplet splittings.

Since the Fe^{2+} and Fe^{3+} L_3 edges are well separated in energy, it is possible to determine Fe^{3+}-Fe^{2+} ratios by fitting reference spectra to the experimental Fe $L_{2,3}$ edges. This has been demonstrated by Cressey et al. (1993) using XANES from a number of Fe-containing minerals having mixed valency and coordination. The same would also be possible using EELS data, as long as a small collection semiangle, β, was used in the microscope, which would ensure that only dipole-allowed transitions were collected. Under this condition, EELS and XAS are equivalent. The success of determining Fe^{3+}-Fe^{2+} ratios by fitting reference spectra in part depends on the constancy of the Fe $L_{2,3}$-edge shapes in different materials and environments. The spectra illustrated in Figures 2 and 3 and published Fe $L_{2,3}$ EELS and XAS spectra (Krishnan, 1990; Krivanek and Paterson, 1990; Kurata et al., 1990; Paterson and Krivanek, 1990; Cressey et al., 1993) indicate that the Fe^{2+} and Fe^{3+} $L_{2,3}$ edges do not show large deviations from the calculated Fe $L_{2,3}$ edge spectra of van der Laan and Kirkman (1992), and so Fe^{3+}-Fe^{2+} ratio determination should be possible for compounds containing Fe^{2+} and Fe^{3+} in roughly tetrahedral and octahedral coordination where the Fe to ligand bonds are dominantly ionic. The crystallinity of the mineral should also have little effect on the shape of the Fe $L_{2,3}$ edges, if one assumes that the metal to ligand bonds are dominantly ionic, since the spectra for Fe^{2+} and Fe^{3+} are dominated by quasi-atomic transitions that give rise to the Fe $L_{2,3}$ edge, with only some modification due to the solid state environment. Fe^{3+}-Fe^{2+} ratio determination is expected to be more difficult when a multivalent or multisite compound contains sites that are highly distorted from T_d or O_h symmetry, as in iron phthalocyanine (Koch et al., 1985), which contains Fe in a square planar site, or when the character of the ligands bonded to the Fe causes the Fe to assume the low-spin state, as in FeS_2 (Thole and van der Laan, 1988) and the iron isocyanates (Kurata et al., 1990). Although Cressey et al. (1993) have shown that it is possible to determine the Fe^{3+}-Fe^{2+} ratio in a number of materials, such as spinels, amphiboles, Fe-containing glass, and amethyst, this implies that one can determine the Fe^{3+}-Fe^{2+} ratio at the nanometer scale using EELS, assuming the energy resolution of the EELS/TEM setup is ~0.5 eV or better. Such an energy resolution is usually only obtained with an ultra-high vacuum TEM fitted with a cold field emission gun.

Mn. Mn is another element common in the geological environment, and chemically it can exhibit a large number of oxidation states and coordinations. In contrast to Fe, Mn is found in the three oxidation states II, III, and IV in nature, although Mn in sedimentary and surficial

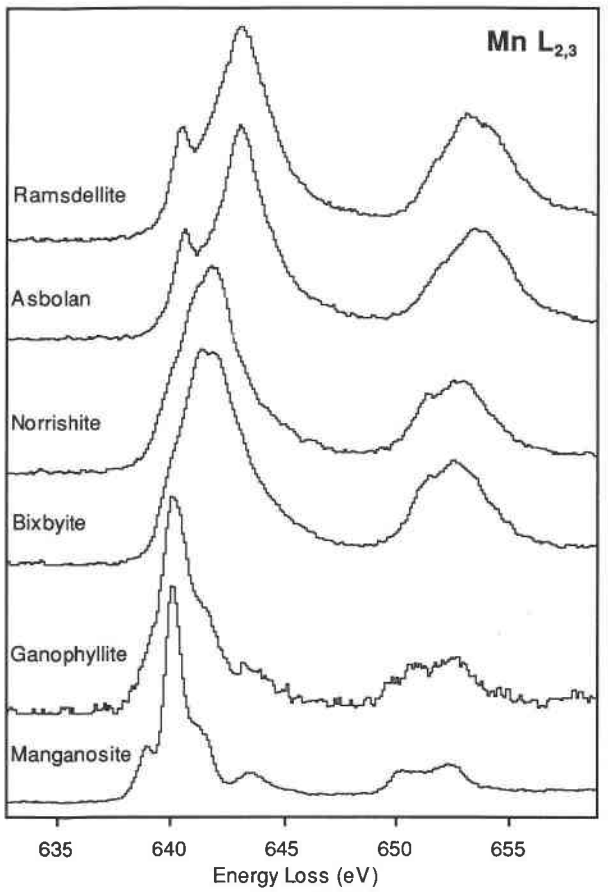

Fig. 4. Mn $L_{2,3}$ edges from representative Mn compounds showing the effect of different oxidation states on the shape and energy of the $L_{2,3}$ edges. Manganosite ($^{[6]}Mn^{2+}$), ganophyllite ($^{[6]}Mn^{2+}$), bixbyite (two distinct $^{[6]}Mn^{3+}$ sites), norrishite (single $^{[6]}Mn^{3+}$ site), asbolan ($^{[6]}Mn^{4+}$), and ramsdellite ($^{[6]}Mn^{4+}$).

Mn minerals is more likely to be Mn^{3+} and Mn^{4+}. The coordination of Mn is almost always octahedral, although $^{[4]}Mn^{2+}$ is found in some minerals such as jacobsite, galaxite, and hausmannite. Mn minerals are often fine-grained heterogeneous mixtures containing more than one oxidation state. That makes the determination of their oxidation state by conventional spectroscopic and chemical techniques very difficult and imprecise, as it only gives a summed average of the oxidation states from the bulk sample. The high spatial and energy resolution offered by PEELS in a FEG-STEM is ideal for obtaining such information.

Figure 4 compares the Mn $L_{2,3}$ edges from a number of Mn-containing minerals. There are three obvious changes in the spectra with an increasing oxidation state of the Mn: a move to higher energy losses of the L_3 peak maximum (Table 3), a decrease in the L_3-L_2 white line intensity ratio, and a characteristic shape change of the $L_{2,3}$ edges. Manganosite illustrates a typical Mn^{2+} $L_{2,3}$ edge with an L_3 peak maximum at ca. 640 eV; many other high-spin Mn^{2+} compounds have been studied previous-

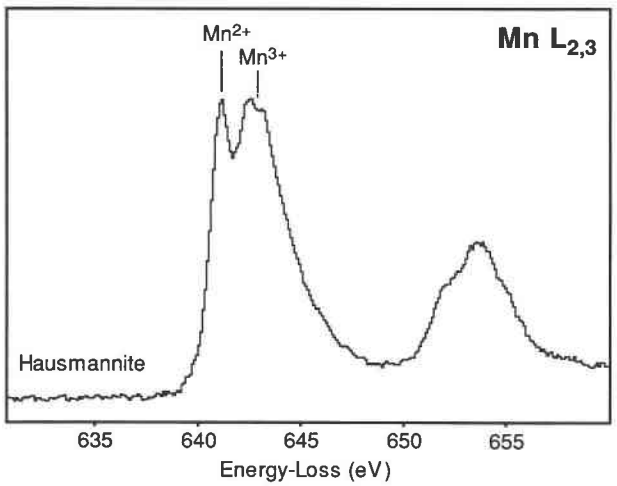

Fig. 5. Mn $L_{2,3}$ edges from a well-crystallized specimen of hausmannite. The L_3 edge is split into two peaks because of the two Mn sites in hausmannite ($^{[4]}Mn^{2+}$ and $^{[6]}Mn^{3+}$).

ly, and all exhibit the same basic edge shape with little variation in coordination number or site symmetry (Rask et al., 1987; Garvie and Craven, 1993). The Mn $L_{2,3}$ edges from ganophyllite have the same shape and L_3 energy as in manganosite, indicating that the Mn is dominantly Mn^{2+}, as is commonly assumed for this mineral (Dunn et al., 1983). The Mn $L_{2,3}$ edges shown here are typical of high-spin $^{[6]}Mn^{2+}$. Low-spin $^{[6]}Mn^{2+}$ is not thought to occur in natural minerals, although it has a characteristic edge shape (Cramer et al., 1991) that can be used to distinguish it from high-spin $^{[6]}Mn^{2+}$. Two minerals are illustrated that contain Mn^{3+}, bixbyite, and the oxybiotite norrishite (Tyrna and Guggenheim, 1991). The Mn $L_{2,3}$ edges in both minerals are very similar in shape, with a broad L_3 edge and a maximum at ca. 642 eV. In bixbyite the L_3 peak maximum is split into two peaks separated by ca. 0.5 eV, and there is further evidence of unresolved multiplet splitting on the low-energy side of the L_3 peak. In norrishite only partially resolved multiplets are observed; this was observed for several Mn^{3+} L_3 edges (Garvie and Craven, 1993) where the Mn sits in a Jahn-Teller distorted environment due to the d^4 electron configuration. The last two examples in Figure 4 are from the Mn^{4+} minerals asbolan and ramsdellite (Miura et al., 1990). As with the Mn^{2+} and Mn^{3+} $L_{2,3}$ edges, the Mn^4 $L_{2,3}$ edges have distinct edge shapes, with an L_3 peak maximum at ca. 644 eV. All Mn^{4+} $L_{2,3}$ edges have similar shapes, with a broad L_2 edge and a double peaked L_3 edge. The two peaks on the L_3 edge have been interpreted in terms of crystal field theory and assigned to the t_{2g} and e_g orbitals, respectively (Garvie and Craven, 1993). Similar assignments were made on the Mn^{2+} L_3 edge. Interpretation of the Mn^{3+} L_3 edge is more complicated because of the tetragonal distortion of the octahedron caused by the Jahn-Teller effect, which further splits the t_{2g} and e_g orbitals. The Mn L_3 edge from manganite was assigned orbitals based on D_{4h} symmetry in Garvie and Craven (1993).

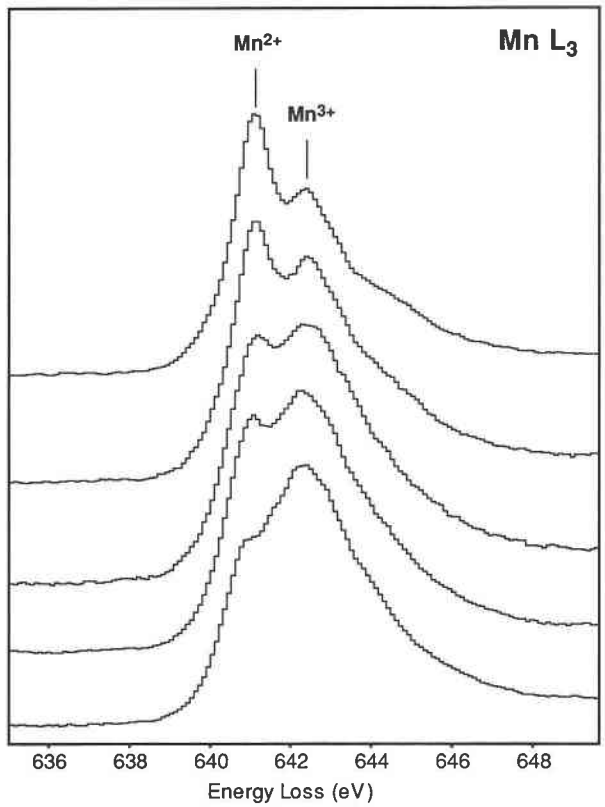

Fig. 6. Representative L_3 edges from another sample of hausmannite. The L_3 edges are arranged from top to bottom with an increase in intensity of the Mn^{3+} peak corresponding to an increase in the relative amount of Mn^{3+}.

The ability of PEELS to observe variations in oxidation state at high spatial resolution was studied in two samples of hausmannite. Both samples occurred as small, octahedral crystals of ~1 mm in size but were from different localities. The first sample gave distinct and similar Mn $L_{2,3}$ edge shapes from all the areas studied under the microscope. Figure 5 illustrates a typical $L_{2,3}$ edge from the first sample. A similar edge shape has been recorded by XANES (Cressey et al., 1993) and ELNES (Paterson and Krivanek, 1990). The Mn L_3 edge from hausmannite can be interpreted by consideration of its crystal structure. Hausmannite can be represented by the formula $^{[4]}Mn^{2+}{}^{[6]}Mn_2^{3+}O_4$ with an ideal Mn^{3+}-Mn^{2+} ratio of 2:1, although experimentally synthesized hausmannite was found to have Mn^{3+}-Mn^{2+} ratios varying from 2 to 3.5 (Kaczmarek and Wolska, 1993). The L_3 edge shows two distinct peaks separated by 1.6 eV. The first one is at 640 eV, consistent with Mn^{2+}, and the second one is ca. 1.5 eV higher and is from Mn^{3+}. The second sample of hausmannite exhibited a range of Mn L_3-edge shapes. Representative spectra are illustrated in Figure 6. It is evident from these spectra that there are large variations in the Mn^{3+}-Mn^{2+} ratio, ranging from almost pure Mn^{2+} (at the top of Fig. 6) to edges that resemble ideal hausmannite (middle of Fig. 6) to edges that are dominated by Mn^{3+}

(bottom of Fig. 6). These variations can occur over distances as short as 100 nm.

Cr. In nature, Cr occurs in two oxidation states, III and VI. The Cr^{6+} ion occurs exclusively in the chromate and dichromate anions, as in crocoite, $PbCrO_4$, and has not been found in clay minerals. The best-known Cr-bearing clay is the smectite volkonskoite, which has a bright green color due to the high percentage of Cr residing in the octahedral layer (Güven, 1988). the Cr $L_{2,3}$ edges for three minerals are illustrated in Figure 7. The Cr $L_{2,3}$ edges from chromite show the same multiplet structure and basic edge shapes as the theoretical atomic multiplet spectra of van der Laan and Kirkman (1992) for Cr^{3+} in O_h symmetry and 10Dq values of 2–2.5 eV. This range of 10Dq values is consistent with the crystal field strength of $^{[6]}Cr^{3+}$ compounds bonded to O that have optically determined 10Dq values of 2.1–2.5 eV (Lever, 1984). The Cr L_3 edge for chromite is at 578.6 eV. When one compares the Cr $L_{2,3}$ edges from volkonskoite and chromite, it is evident that the various features have the same shape and energy positions. This directly confirms the trivalent nature of Cr in the volkonskoite. The features on the L_3 edge in the volkonskoite are slightly broader than those from the chromite, which can possibly be attributed to the more distorted octahedral environment in the former mineral. Similar edge shapes have been recorded previously for the Cr $L_{2,3}$ edges from Cr_2O_3 (Kurata et al., 1988; Krivanek and Paterson, 1990). For comparison, the Cr $L_{2,3}$ edge from crocoite is illustrated in Figure 7. This edge is consistent with lower energy resolution PEELS work on K_2CrO_4 (Kurata et al., 1988). The L_3 and L_2 edges are resolved into two separate peaks, and there is a shift of the L_3 peak maximum to a higher energy loss (Table 3), consistent with the higher effective charge on the Cr atom. The $^{[4]}Cr^{6+}$ $L_{2,3}$-edge shape is characteristic of tetrahedrally coordinated XO_4^{n-} anions (X = Ti, V, Cr, and Mn) in general (Brydson et al., 1993) and provides a fingerprint for these species.

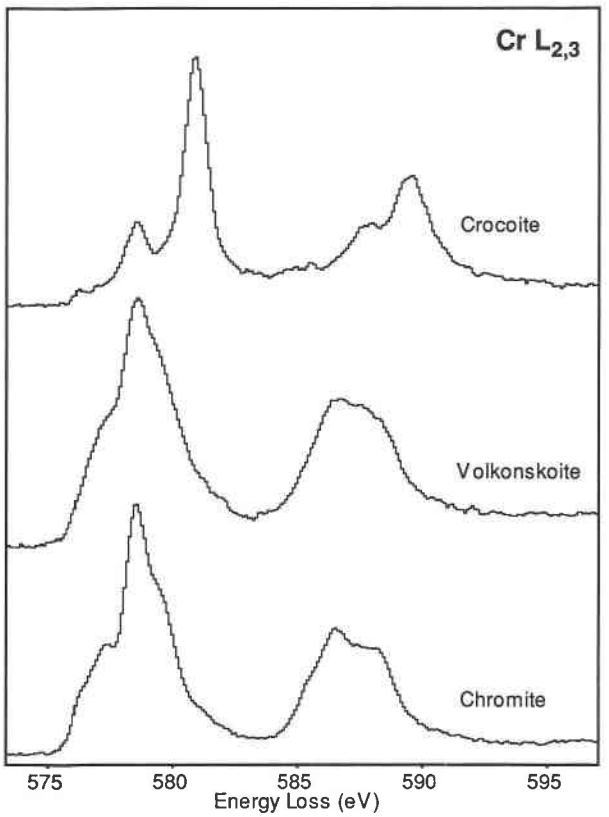

Fig. 7. Cr $L_{2,3}$ edges for chromite ($^{[6]}Cr^{3+}$), volkonskoite ($^{[6]}Cr^{3+}$), and crocoite ($^{[4]}Cr^{6+}$).

Anion and cation coordination fingerprints

Many EELS spectra exhibit a near-edge structure characteristic of the arrangement and number of atoms in the first coordination shell surrounding an atom. This gives rise to the concept of a coordination fingerprint (Brydson et al., 1988; Sauer et al., 1993). A coordination fingerprint arises when the excited atom is surrounded by atoms that are strong electron backscatterers, such as O^{2-} and F^-. In that case the near-edge structure is dominated by scattering events within the first coordination shell surrounding the atom. The ELNES structure may then be related to the molecular orbital (MO) structure of the excited atom and its nearest neighbors (Sauer et al., 1993). Some examples of ELNES coordination fingerprints include the B K edge from BO_3 and BO_4 (Sauer et al., 1993), the S and P K edges from SO_4^{2-} and PO_4^{3-} anions (Hofer and Golob, 1987), the $L_{2,3}$ and K edges from $^{[4]}Al$ and $^{[6]}Al$ (Brydson et al., 1989b; Ildefonse et al., 1992), and the K edges of $^{[4]}Mg$ and $^{[6]}Mg$ (Taftø and Zhu, 1982).

Several allotropes of C exist, the most well known being diamond, graphite, and the fullerenes such as C_{60}. Between the extremes of sp^3-bonded diamond and sp^2-bonded graphite are a whole range of carbonaceous materials that have intermediate bond types, such as glassy C and evaporated amorphous C (Robertson, 1986; Robertson and O'Rielly, 1987). In minerals, inorganically bonded C is found almost exclusively in the carbonate anion, CO_3^{2-}. Its structure consists of a central C atom that is bonded to three planar trigonal O atoms. The CO_3^{2-} anion is isostructural and isoelectronic with BO_3^{3-} and NO_3^- anions, which all exhibit similar K ELNES shapes. The C K ELNES from the minerals containing the carbonate anion exhibit an edge shape consisting of a sharp initial peak at 290.2 eV and a broader, less intense, feature with a maximum at 301.3 eV (Fig. 8). These features may be attributed to transitions to the unoccupied π^* and σ^* antibonding molecular orbitals of a CO_3^{2-} cluster, respectively. The C K edge from the CO_3^{2-} anion is illustrated for calcite, siderite, and two members of the hydrotalcite group, hydrotalcite and desautelsite (Fig. 8). The extra structure on the σ^* peak from calcite is probably due to scattering from shells surrounding the carbonate cluster. For comparison, Figure 8 illustrates the C K edge for evaporated amorphous C, graphite, and diamond. Their edges are consistent with previously pub-

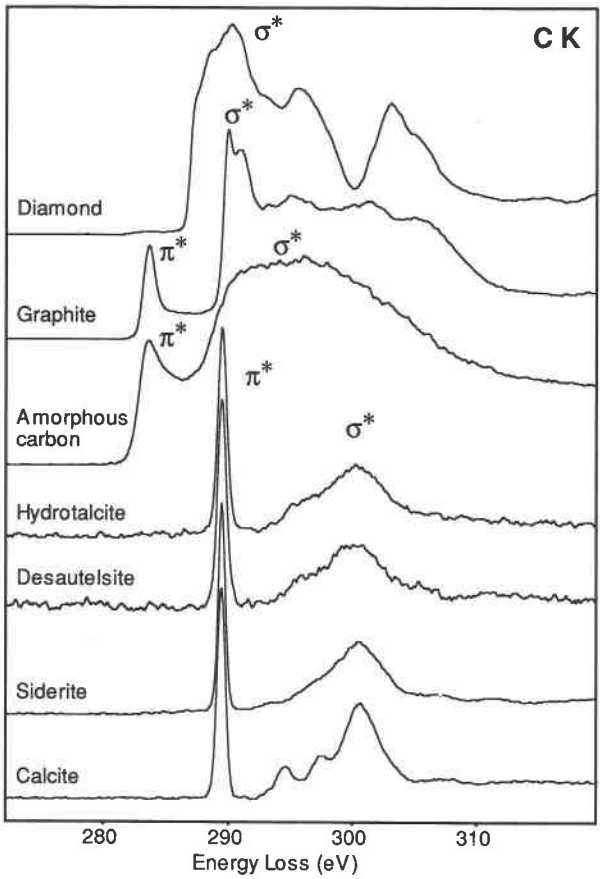

Fig. 8. C *K* edge from minerals containing the carbonate anion (calcite, siderite, desautelsite, and hydrotalcite) and three allotropes of C (amorphous C, graphite, and diamond).

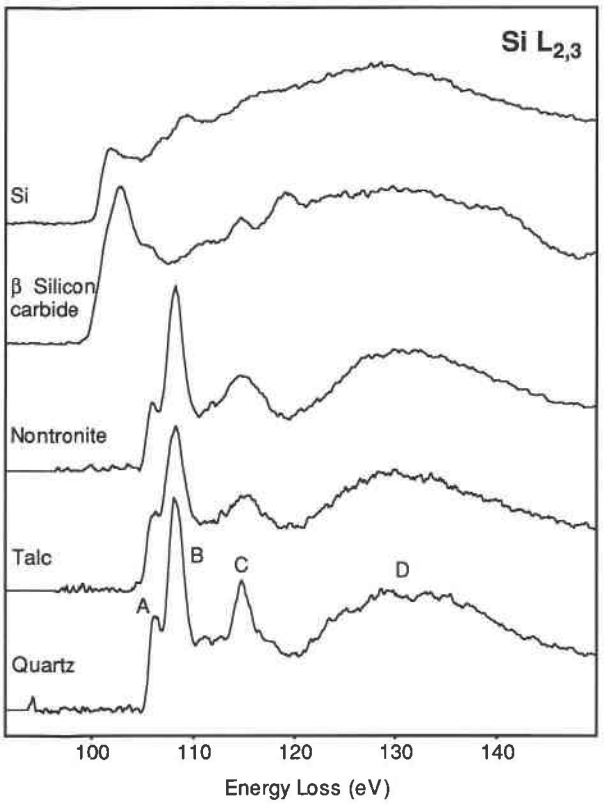

Fig. 9. Si $L_{2,3}$ edges from three silicates containing SiO_4 tetrahedra (quartz, talc, and nontronite). For comparison, the Si $L_{2,3}$ edges from β-SiC and Si are also shown.

lished XANES and ELNES for these materials (Kincaid et al., 1978; Rosenberg et al., 1986; Berger et al., 1988; Weng et al., 1989a; Bernatowicz et al., 1990; Batson and Bruley, 1991; Katrinak et al., 1992). The fullerenes C_{60} and C_{70} also have C *K* edge shapes similar to that from graphite but with differences due to the molecular nature of the C_{60} and C_{70} molecules (Terminello et al., 1991; Shinohara et al., 1991). Amorphous C and graphite have basically the same edge shapes, with an initial peak at 285 eV and a second more intense feature at ca. 290 eV; the similarities can be explained in terms of the similarities in their bonding. Diamond has a different edge shape from graphite, with a peak maximum at 292.6 eV. The differences between the C *K* edges in graphite and diamond may be explained by the presence of sp^2 bonding in graphite, which results in a peak at 285 eV, identified as transitions to the π^* molecular orbital, and a second peak at 290 eV, due to transitions to σ^* orbitals (Weng et al., 1989a). In diamond the bonding between the C atoms can be explained in terms of tetrahedrally directed sp^3 hybrid orbitals, and the first peak is identified as arising from transitions to molecular orbitals of σ^* character (Weng et al., 1989a).

The presence of Si in minerals is almost exclusively associated with the SiO_4 tetrahedron. These tetrahedra may join together to form a large number of crystalline silica polymorphs (Keskar and Chelikowsky, 1992), as well as amorphous and glassy phases. The silicates are also characterized by the SiO_4 tetrahedron: these tetrahedra are present in simple isolated tetrahedra, as in the neosilicates, but also join together to form a huge number of structures (Liebau, 1985). A common cation fingerprint observed in minerals is the Si $L_{2,3}$ edge from $^{[4]}$Si. The Si $L_{2,3}$ edges from quartz, talc, and nontronite are illustrated in Figure 9, together with the Si $L_{2,3}$ edges from Si and SiC. The Si $L_{2,3}$ edges from quartz and the two clay minerals exhibit very similar edge shapes, characterized by two initial sharp peaks, peaks A (106.3) and B (108.4 eV), followed by a sharp peak C (115.0) and a broad peak D (ca. 133 eV). Peak A, from quartz, is split into two peaks separated by 0.45 eV; a similar splitting has been recorded by high-resolution XANES (Li et al., 1993) and EELS (Garvie, unpublished data). The observed structures have been assigned to the unoccupied molecular orbitals of a SiO_4^{4-} tetrahedron (McComb et al., 1991; Li et al., 1993). Thus based on the molecular orbital assignments in McComb et al. (1991) and Li et al. (1993), the four peaks from the quartz Si $L_{2,3}$ edge have been assigned to the following unoccupied molec-

ular orbitals: peak A = a_1 (s-like), peak B = t_2 (p-like), peak C = primarily e (d-like), and peak D = t_2 (d-like). This Si $L_{2,3}$-edge shape is seen in the majority of silicates, although a recent study of the neosilicates (McComb et al., 1991, 1992) illustrates that the fingerprint technique must be used with care. Relative to quartz, the Si $L_{2,3}$ ELNES from zircon (McComb et al., 1992) shows a distinctly different edge shape, which is related to the highly distorted SiO_4^{4-} tetrahedra. Octahedrally coordinated Si, which rarely occurs in minerals, is present in stishovite. The Si $L_{2,3}$ absorption edge from stishovite (Li et al., 1993) is considerably different in shape from the Si $L_{2,3}$ ELNES in minerals containing regular or distorted SiO_4 tetrahedra, which implies that the edge shape may be used as a guide to the coordination of the Si. The different Si $L_{2,3}$ ELNES from minerals containing regular or distorted SiO_4 tetrahedra could possibly be used as a guide to the site symmetry of the Si, although further experimental work will be needed to confirm this. For comparison, the $L_{2,3}$ edges from SiC and Si are illustrated in Figure 9. The differences in the edge shapes between the Si $L_{2,3}$ edges from the silicates and the Si and SiC can be understood in terms of the differing unoccupied densities of states (Weng et al., 1989b, 1990), whereas the different positions of the edge onsets are related to the differing effective charges on the Si atoms in the different materials.

Modeling core-loss edges

A host of theoretical techniques have been used to model EELS core-loss edges, which can be divided roughly into two types (de Groot et al., 1993): the local density approximation (LDA) and the ligand field multiplet (LFM) approaches. The former includes methods such as band structure, multiple scattering, and molecular orbital calculations (see Brydson, 1991, for an introduction to these methods as applied to ELNES data). These are suitable for weakly correlated systems where the interaction of the excited electron with the core hole created by the excitation process is small. The LFM method explicitly takes account of electron-electron and electron-core hole interactions in strongly correlated systems and has been most successfully used to model the 3d transition metal $L_{2,3}$ edges (de Groot et al., 1990a, 1990b; van der Laan and Kirkman, 1992; Cressey et al., 1993) and $M_{2,3}$ edges (van der Laan, 1991). Two contrasting methods for modeling the different core-loss edges in MnO are illustrated: the multiple scattering method to model the O K edge and the atomic multiplet method for the Mn $L_{2,3}$ edge.

Multiple scattering calculations

The multiple scattering calculations were performed using the ICXANES computer code of Vvedensky et al. (1986) using full multiple scattering. Multiple scattering theory is based on the interference between the outgoing ejected electron wave and the returning backscattered electron wave. Briefly, the transition rate of excitation is calculated within the dipole approximation, using essentially an atomic contribution modified by multiple elastic

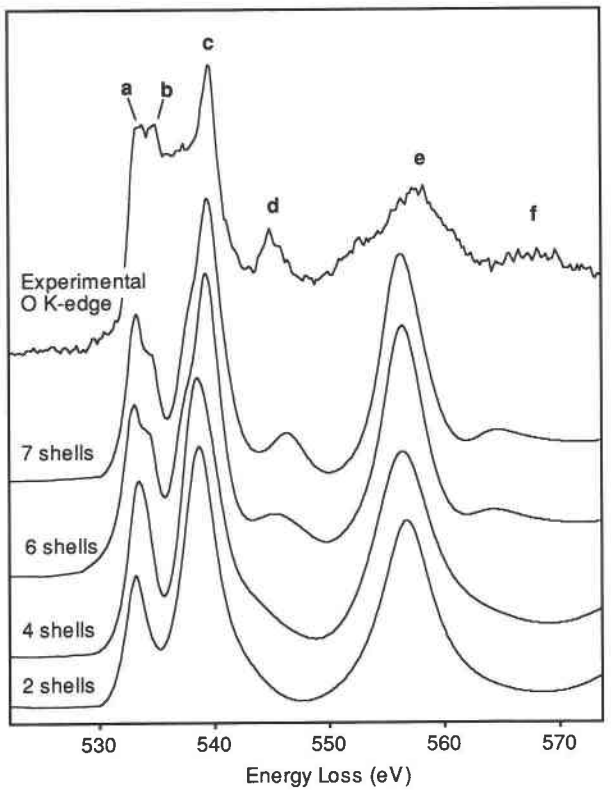

Fig. 10. Experimental O K edge from MnO compared with the results of the multiple scattering calculations for different cluster sizes. The results for shells 3 and 5 are not illustrated, as they had little effect on the final plot.

scattering of the excited electron by the surrounding atoms. This approach, while formally equivalent to a Korringa-Kohn-Rostocker band structure calculation, is considerably more flexible, allowing the inclusion of excited atom potentials to account for the effects of the excitation process. The scattering properties of the various atoms are described by phase shifts that may be calculated by numerical integration of the Schrödinger equation, assuming a muffin-tin form for the atomic potentials in the crystal, obtained by the simple superposition of neutral atomic charge densities. The multiple scattering calculation is performed in real space by dividing the cluster into shells of atoms surrounding the central excited atom. The multiple scattering is solved within each shell in turn, and the results are then combined to reassemble the final cluster, use being made of any structural symmetry.

Many studies have illustrated the applicability of the multiple scattering approach in modeling ELNES and XANES spectra (Oizumi et al., 1985; Lindner et al., 1986; Brydson et al., 1988, 1992b; McComb et al., 1992; Sipr, 1992; Kurata et al., 1993). The calculations for the O K edge in MnO (Fig. 10) were performed for seven shells, extending to a cluster radius of 11.86 au (where 1 au = 0.52918 Å) around an O atom. The core hole was accounted for by the use of the $(Z + 1)^*$ approximation for

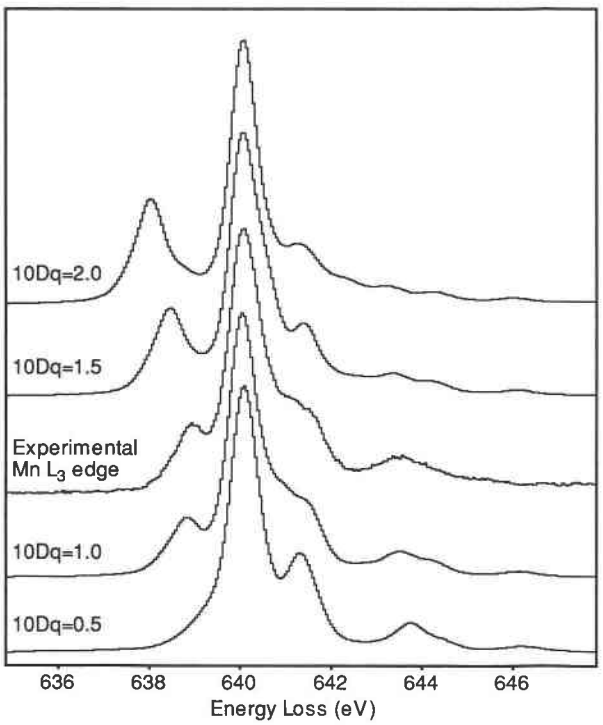

Fig. 11. Comparison of the Mn L_3 edge from manganosite ($^{[6]}Mn^{2+}$) with the calculated Mn d^5 atomic multiplet spectra for Mn^{2+} in O_h symmetry with crystal field strengths of 0.5–2.0 eV.

the central O atom in the cluster. In agreement with the findings of Lindner et al. (1986) and Rez et al. (1991) on MgO, the dominant scatterers in oxide structures are the O atoms, and it is possible to reproduce many of the major features using a cluster that ignores the Mn atoms. The following cluster surrounding a central O atom was used: shell 1 = six Mn atoms at 4.19 au, shell 2 = 12 O atoms at 5.93 au, shell 3 = eight Mn atoms at 7.26 au, shell 4 = six O atoms at 8.38 au, shell 5 = 24 Mn atoms at 9.37 au, shell 6 = 24 O atoms at 10.27 au, and shell 7 = 12 O atoms at 11.86 au. By varying the cluster size, the features in the experimental O *K* edge can be assigned to specific scattering events. The six main features of the experimental O *K* edge, labeled a–f, are successfully reproduced by the multiple scattering calculation (Fig. 10). The first peak, a, can be adequately reproduced using solely the first coordination shell (shell 1) of Mn. The dominant scattering events are d-like scattering from Mn and p-like scattering from O. Hence this feature reflects transitions to unoccupied O 2p states hybridized with the narrow metal 3d band that is highly localized around the metal atom sites. This region therefore reflects the covalence in the transition metal oxides. This is in agreement with the previous work on the O *K* edges of 3d transition metal compounds (de Groot et al., 1989; Kurata et al., 1993). Peak b appears to arise only after inclusion of a third O shell (sixth coordination shell) indicating that this region is also sensitive to longer range effects. The sharp intense peak c arises because of intrashell multiple scattering within the first O coordination shell and reflects transitions to unoccupied O 2p states hybridized with the more delocalized Mn 4s and 4p states. Peaks d and f are adequately reproduced after the addition of a third O coordination shell (shell 6) and arise from mainly intershell multiple scattering. Finally, the large broad peak e is modeled using the first O coordination shell and may be adequately reproduced using solely single scattering. Such a basic resonant feature is known as a multiple scattering resonance, and its energy position follows the relationship $E \propto 1/R^2$ (where E is the energy of the feature above the edge onset and R is the O-O distance). Thus such multiple scattering resonances provide a means of determining bond lengths and bond length variations (Kurata et al., 1993). Multiple scattering resonances arise since certain ions (notably the oxide anion) are relatively strong backscatterers and give rise to a potential barrier for electron scattering.

Atomic multiplet calculations

The 3d transition metal $L_{2,3}$ edges cannot be modeled in terms of a one particle density of states because of the large electron correlation effects in the partially filled 3d orbitals and the strong interaction with the 2p core hole created during the excitation process. The LFM approach has been used to model the $L_{2,3}$ edges in a number of 3d transition metals and compounds (de Groot et al., 1990a, 1990b; van der Laan and Kirkman, 1992). The theoretical Mn^{2+} $L_{2,3}$ data presented here were calculated by van der Laan and Kirkman (1992) and take account of the following effects in order to calculate the $2p^63d^n \rightarrow 2p^53d^{n+1}$ dipole transitions: 2p-3d and 3d-3d Coulomb and exchange interactions, 2p and 3d spin-orbit interactions, and the crystal field acting on the 3d states. Although transitions 2p → 4s are dipole allowed, they have been neglected in the calculations because the 2p → 3d transitions dominate over the transitions to 4s states. The 3d-3d and 2p-3d two particle interactions define the ground state of the transition metal ion and split the EELS-XAS final state into a large number of configurations. The calculated atomic multiplet spectrum for the $3d^n$ compounds ($n > 0$) typically consists of hundreds of unresolvable final states spread over typically 15 eV for the Mn $L_{2,3}$ edges. In order to compare the multiplet spectra with experimental ones, the multiplet lines are broadened to take into account effects such as lifetime and vibrational broadening and hybridization.

The validity of the atomic multiplet method to model the experimental $L_{2,3}$ edge is illustrated in Figure 11. In this figure the theoretical multiplet spectra for Mn^{2+} in O_h symmetry with crystal field values of 0.5, 1, 1.5, and 2 eV are compared with the Mn L_3 edge from MnO. The agreement between the experimental L_3 edge and the theoretical L_3 edge with a crystal field value of 1 eV is excellent. All the features on the experimental edge are reproduced in the theoretical spectrum. This crystal field value of ca. 1 eV, determined by comparing the experi-

mental L_3 edge with the theoretical ones, is also in good agreement with the 10Dq of 1.2 eV (Pratt and Coehlo, 1959) determined for MnO by optical spectroscopy. The good agreement between the theoretical and experimental Mn L_3 edge for MnO is in part due to the dominantly ionic bonding between Mn and O. For more covalent compounds such as Mn-O bonding in pyrolusite, the experimental and theoretical edges show quite different structures (Garvie and Craven, 1993, 1994). Most theoretical atomic multiplet spectra calculations assume solely ionic-type bonding, although introducing terms in the calculations for covalence can be used successfully to model more covalent compounds (van der Laan et al., 1986), but this is more difficult.

Effects induced by the electron beam

In minerals, the main effects of electron beam irradiation are element mobility and amorphization (Champness and Devenish, 1992). These effects are most notable during EDX in a TEM, where element mobility and loss is often a major problem, particularly with the long counting times required for EDX. These problems can be especially acute for the clay minerals (van der Pluijm et al., 1988), which often contain mobile elements such as K, as well as H_2O and OH. In many instances the effects induced by the electron beam change the nature of the solid and therefore also the environment of specific atoms. These changes can be followed using an atom-specific probe such as PEELS. PEELS has been used to follow the changes occurring during the electron irradiation of solids, such as the transformation of calcite to CaO (Walls and Tencé, 1989; Murooka and Walls, 1991) and the transformation of BO_4 to BO_3 in hydroxyborates (Sauer et al., 1993). Egerton et al. (1987) provided a good overview of PEELS-related studies of chemical changes induced by the electron beam. In materials containing 3d transition elements, the changes in the edge shape are consistent with changes in the valency of the transition metal atom. This has been studied in detail in the mineral asbolan (Garvie and Craven, 1994), where it was possible to follow the reduction of the Mn^{4+} to Mn^{2+} with intense electron beam irradiation. During irradiation the Mn $L_{2,3}$ edge changes its shape and position, consistent with increasing proportions of Mn^{3+} and finally Mn^{2+}.

Although the majority of materials containing Mn in the oxidation states of III or IV were found to be reduced to lower oxidation states, the opposite has occasionally been observed. In sussexite, $Mn^{2+}BO_2(OH)$, and ganophyllite, the L_3 edge initially changed in shape and energy from an Mn^{2+} to an Mn^{3+} L_3 edge. Further irradiation caused the Mn^{3+} edge to revert back to an Mn^{2+} edge. Similar behavior was observed in all the phyllosilicates that contained Fe^{2+}. After a short period of irradiation, the Fe^{2+} component was completely transformed to an L_3 edge having the same energy and shape as $^{[6]}Fe^{3+}$. The oxidation of the Fe^{2+} in the phyllosilicates and the Mn^{2+} in sussexite and ganophyllite is presumably linked to the loss of H in the OH anions, which is expected to be very mobile under the electron beam, and subsequent oxidation of the metal.

Acknowledgments

We are all grateful to the following for providing samples: G.C. Allen (Interface Analysis Centre, University of Bristol, U.K.) for the synthetic jacobsite; D.C. Bain (Macaulay Land Use Research Institute, U.K.) for the samples of volkonskoite and daphnite; J. Faithfull (Hunterian Museum, U.K.) for samples of ganophyllite (M9609), hausmannite (M8097), and silicon carbide; H.C.B. Hansen (Royal Veterinary and Agricultural University, Denmark) for the synthetic desautelsite; C.M.B. Henderson (Department of Geology, University of Manchester, U.K.) for the synthetic iron analogue of leucite; S. Guggenheim (University of Illinois at Chicago) for the sample of norrishite; and H. Miura (Department of Geology and Mineralogy, Hokkaido University, Japan) for the ramsdellite. We are grateful to G. van der Laan (SERC Daresbury Laboratory, U.K.) for the Mn $L_{2,3}$ multiplet data. The authors would like to thank the SERC for providing the Gatan 666 PEELS and for a postdoctoral research assistantship (L.A.J.G.) under grant GR/G12832.

References cited

Bailey, S.W. (1988) Structures and compositions of other trioctahedral 1:1 phyllosilicates. Mineralogical Society of America Reviews in Mineralogy, 19, 169–188.

Batson, P.E., and Bruley, J. (1991) Dynamic screening of the core exciton by swift electrons in electron-energy-loss scattering. Physical Review Letters, 67, 350–353.

Berger, S.D., McKenzie, D.R., and Martin, P.J. (1988) EELS analysis of vacuum arc-deposited diamond-like films. Philosophical Magazine Letters, 57, 285–290.

Bernatowicz, T.J., Gibbons, P.C., and Lewis, R.S. (1990) Electron energy loss spectrometry of interstellar diamonds. The Astrophysical Journal, 359, 246–255.

Bonnin, D., Calas, G., Suquet, H., and Pezerat, H. (1985) Sites occupancy of Fe^{3+} in Garfield nontronite: A spectroscopic study. Physics and Chemistry of Minerals, 12, 55–64.

Brydson, R. (1991) Interpretation of near-edge structure in the electron energy-loss spectrum. Bulletin of the Electron Microscopy Society of America, 21, 57–67.

Brydson, R., Williams, B.G., Engel, W., Sauer, H., Zeitler, E., and Thomas, J.M. (1987) Electron energy-loss spectroscopy (EELS) and the electronic structure of titanium dioxide. Solid State Communications, 64, 609–612.

Brydson, R., Williams, B.G., Engel, W., Lindner, Th., Muhler, M., Schlögl, R., Zeitler, E., and Thomas, J.M. (1988) Electron energy-loss spectroscopy and the crystal chemistry of rhodizite. II. Near-edge structure. Journal of the Chemical Society, Faraday Transactions 1, 84, 631–646.

Brydson, R., Sauer, H., Engel, W., Thomas, J.M., Zeitler, E., Kosugi, N., and Kuroda, H. (1989a) Electron energy loss and x-ray absorption spectroscopy of rutile and anatase: A test of structural sensitivity. Journal of Physics: Condensed Matter, 1, 797–812.

Brydson, R., Sauer, H., Engel, W., Thomas, J.M., and Zeitler, E. (1989b) Co-ordination fingerprints in electron loss near-edge structures: Determination of the local site symmetry of aluminium and beryllium in ultrafine minerals. Journal of the Chemical Society, Chemical Communications, 15, 1010–1011.

Brydson, R., Sauer, H., and Engel, W. (1992a) Electron energy loss near-edge structure as an analytical tool: The study of minerals. In M.M. Disko, C.C. Ahn, and B. Fultz, Eds., Transmission electron energy loss spectrometry in materials science, p. 131–154. The Minerals, Metals and Materials Society, Warrendale, Illinois.

Brydson, R., Sauer, H., Engel, W., and Hofer, F. (1992b) Electron energy-loss near-edge structures at the oxygen *K*-edges of titanium (IV) oxygen compounds. Journal of Physics: Condensed Matter, 4, 3429–3437.

Brydson, R., Garvie, L.A.J., and Craven, A.J. (1993) $L_{2,3}$-edges of tetrahedrally co-ordinated d^0 transition metal oxoanions XO_4^{n-}. Journal of Physics: Condensed Matter, 5, 9379–9392.

Buechner, U. (1975) The dielectric function of mica and quartz deter-

mined by electron energy losses. Journal of Physics C: Solid State Physics, 8, 2781–2787.

Buseck, P.R., and Self, P. (1992) Electron energy loss spectroscopy (EELS) and electron channelling (ALCHEMI). Mineralogical Society of America Reviews in Mineralogy, 27, 141–180.

Calas, G. (1988) Electron paramagnetic resonance. Mineralogical Society of America Reviews in Mineralogy, 18, 513–571.

Calas, G., and Petiau, J. (1983) Coordination of iron in oxide glasses through high resolution K-edge spectra: Information from the pre-edge. Solid State Communications, 48, 625–629.

Cardile, C.M., and Brown, I.W.M. (1988) An ^{57}Fe Mössbauer spectroscopic and X-ray diffraction study of New Zealand glauconite. Clay Minerals, 23, 13–25.

Champness, P.E., and Devenish, R.W. (1992) Radiation damage in silicate minerals: Implications for AEM. In A. López-Galindo and M.I. Rodríguez-García, Eds., Electron microscopy 92, vol. II: Materials sciences, p. 541–545. Secretariado de Publicaciones de la Universidad de Granada, Granada, Spain.

Colliex, C., Manoubi, T., Gasgnier, M., and Brown, L.M. (1985) Near edge fine structures on electron energy loss spectroscopy core-loss edges. Scanning Electron Microscopy, II, 489–512.

Cramer, S.P., de Groot, F.M.F., Ma, Y., Chen, C.T., Sette, F., Kipke, C.A., Eichhorn, D.M., Chan, M.K., Armstrong, W.H., Libby, E., Christou, G., Brooker, S., McKee, V., Mullins, O.C., and Fuggle, J.C. (1991) Ligand field strengths and oxidation states from manganese L-edge spectroscopy. Journal of the American Chemical Society, 113, 7937–7940.

Cressey, G., Henderson, C.M.B., and van der Laan, G. (1993) Use of L-edge X-ray absorption spectroscopy to characterise multiple valence states of 3d transition metals: A new probe for mineralogical and geochemical research. Physics and Chemistry of Mineral, 20, 111–119.

de Groot, F.M.F., Grioni, M., Fuggle, J.C., Ghijsen, J., Sawatzky, G.A., and Petersen, H. (1989) Oxygen 1s x-ray-absorption edges of transition-metal oxides. Physical Review, B40, 5715–5723.

de Groot, F.M.F., Fuggle, J.C., Thole, B.T., and Sawatzky, G.A. (1990a) $L_{2,3}$ x-ray-absorption edges of d^0 compounds: K^+, Ca^{2+}, Sc^{3+}, and Ti^{4+} in O_h (octahedral) symmetry. Physical Review, B41, 928–937.

——— (1990b) 2p x-ray absorption of 3d transition-metal compounds: An atomic multiplet description including the crystal field. Physics Review, B42, 5459–5468.

de Groot, F.M.F., Abbate, M., van Elp, J., Sawatzky, G.A., Ma, Y.J., Chen, C.T., and Sette, F. (1993) Oxygen 1s and cobalt 2p x-ray absorption of cobalt oxides. Journal of Physics: Condensed Matter, 5, 2277–2288.

Dunn, P.J., Peacor, D.R., Nelen, J.E., and Ramik, R.A. (1983) Ganophyllite from Franklin, New Jersey; Pajsberg, Sweden; and Wales: New chemical data. Mineralogical Magazine, 47, 563–566.

Egerton, R.F. (1986) Electron energy-loss spectroscopy in the electron microscope, 410 p. Plenum, New York.

Egerton, R.F., Crozier, P.A., and Rice, P. (1987) Electron energy-loss spectroscopy and chemical change. Ultramicroscopy, 23, 305–312.

Garvie, L.A.J., and Craven, A.J. (1993) Determination of the crystal field strength in manganese compounds by parallel electron energy loss spectroscopy. In A.J. Craven, Ed., Proceedings of the Institute of Physics Electron Microscopy and Analysis Group, vol. 138, p. 31–34. Institute of Physics Conference Series, Bristol, U.K.

——— (1994) Electron beam induced reduction of Mn^{4+} in manganese oxides as revealed by parallel EELS. Ultramicroscopy, in press.

Goodman, B.A., and Bain, D.C. (1979) Mössbauer spectra of chlorites and their decomposition products. Proceedings of the International Clay Conference 1978, p. 65–74.

Güven, N. (1988) Smectites. Mineralogical Society of America Reviews in Mineralogy, 19, 497–559.

Hawthorne, F.C. (1988) Mössbauer spectroscopy. Mineralogical Society of America Reviews in Mineralogy, 18, 255–340.

Hofer, F., and Golob, P. (1987) New examples from near-edge fine structures in electron energy loss spectroscopy. Ultramicroscopy, 21, 379–384.

Ildefonse, P., Calas, G., Kirkpatrick, R.J., Montez, B., Flank, A.M., and Lagarde, P. (1992) Local environment of aluminium in amorphous alumino-silicates by XANES and MAS NMR. In Y.K. Kharaka and A.S. Maest, Eds., Proceedings of the 7th International Symposium on Water-Rock Interaction, p. 153–158. Balkema, Rotterdam, Germany.

Joy, D.C. (1993) Electron specimen interactions. In A.G. Fitzgerald, B.E. Storey, and D. Fabian, Eds., Quantitative microbeam analysis, p. 213–245. SUSSP and IOP, Edinburgh and London.

Kaczmarek, J., and Wolska, E. (1993) Cation and vacancy distribution in nonstoichiometric hausmanite. Journal of Solid State Chemistry, 103, 387–393.

Katrinak, K.A., Rez, P., and Buseck, P.R. (1992) Structural variations in individual carbonaceous particles from an urban aerosol. Environmental Science and Technology, 26, 1967–1976.

Keskar, N.R., and Chelikowsky, J.R. (1992) Structural properties of nine silica polymorphs. Physical Review B, 46, 1–13.

Kincaid, B.M., Meixner, A.E., and Platzman, P.M. (1978) Carbon K edge in graphite measured using electron-energy-loss spectroscopy. Physical Review Letters, 40, 1296–1299.

Koch, E.E., Jugnet, Y., and Himpsel, F.J. (1985) High-resolution soft x-ray excitation spectra of 3d-metal phthalocyanines. Chemical Physics Letters, 116, 7–11.

Koster, A.S., and Mendel, H. (1970) X-ray $K\beta$ emission spectra and energy levels of compounds of 3d-transition metals: I. Oxides. Journal of Physics and Chemistry of Solids, 31, 2511–2522.

Krishnan, K.M. (1990) Iron $L_{3,2}$ near-edge fine structure studies. Ultramicroscopy, 32, 309–311.

Krivanek, O.L. (1989) Improved parallel-detection electron-energy-loss spectrometer. Ultramicroscopy, 28, 118–121.

Krivanek, O.J., and Paterson, J.H. (1990) ELNES of 3d transition-metal oxides. I. Variations across the periodic table. Ultramicroscopy, 32, 313–318.

Krivanek, O.L., Ahn, C.C., and Keeney, R.B. (1987) Parallel detection electron spectrometer using quadrupole lenses. Ultramicroscopy, 22, 103–116.

Kurata, H., Ishizuka, K., and Kobayashi, T. (1988) Near edge structure in electron energy loss spectra of chromium trioxide intercalated into graphite and some chromium oxides. Bulletin of the Institute of Chemical Research, Kyoto University, 66, 572–579.

Kurata, H., Nagai, K., Isoda, S., and Kobayashi, T. (1990) ELNES of iron compounds. In L.D. Peachey and D.B. Williams, Eds., Proceedings of the XIIth International Congress for Electron Microscopy, vol. 2: Analytical Sciences, p. 28–29. San Francisco Press, San Francisco, California.

Kurata, H., Lefèvre, E., Colliex, C., and Brydson, R. (1993) ELNES structures in the oxygen K-edge spectra of transition metal oxides. Physical Review, B47, 13763–13768.

Lever, A.B.P. (1984) Inorganic electronic spectroscopy: Studies in physical and theoretical chemistry, vol. 33 (2nd edition), 863 p. Elsevier, Amsterdam.

Li, D., Bancroft, G.M., Kasrai, M., Fleet, M.E., Feng, X.H., Tan, K.H., and Yang, B.X. (1993) High-resolution Si K- and $L_{2,3}$-edge XANES of α-quartz and stishovite. Solid State Communications, 87, 613–617.

Liebau, F. (1985) Structural chemistry of the silicates: Structure, bonding, and classification, 347 p. Springer-Verlag, Berlin.

Lindner, Th., Sauer, H., Engel, W., and Kambe, K. (1986) Near-edge structure in electron-energy loss spectra of MgO. Physical Review B, 33, 22–24.

Manceau, A., Gorshkov, A.I., and Drits, V.A. (1992) Structural chemistry of Mn, Fe, Co, and Ni in manganese hydrous oxides. I. Information from XANES spectroscopy. American Mineralogist, 77, 1133–1143.

Marusak, L.A., Messier, R., and White, W.B. (1980) Optical absorption spectrum of hematite, α-Fe_2O_3 near Ir to UV. Journal of Physics and Chemistry of Solids, 41, 981–984.

McComb, D.W., Hansen, P.L., and Brydson, R. (1991) A study of silicon ELNES in neosilicates. Microscopy, Microanalysis, Microstructures, 2, 561–568.

McComb, D.W., Brydson, R., Hansen, P.L., and Payne, R.S. (1992) Qualitative interpretation of electron energy-loss near-edge structure in natural zircon. Journal of Physics: Condensed Matter, 4, 8363–8374.

McGibbon, A.J. (1991) The application of PEELS on a STEM to the problem of inert gas bubbles in solids. In F.J. Humphreys, Ed., Pro-

ceedings of the Institute of Physics Electron Microscopy and Analysis Group conference, p. 109–112. Institute of Physics Conference Series no. 119, Institute of Physics, Bristol.

Miura, H., Kudou, H., Choi, J.H., and Hariya, Y. (1990) The crystal structure of ramsdellite from Pirika mine. Journal of the Faculty of Science, Hokkaido University, Series IV, 22, 611–617.

Murooka, Y., and Walls, M.G. (1991) Beam damage on anisotropic materials ($CaCO_3$) in STEM. In F.J. Humphreys, Ed., Proceedings of the Institute of Physics Electron Microscopy and Analysis Group conference, p. 337–340. Institute of Physics Conference Series no. 119, Institute of Physics, Bristol.

Oizumi, H., Fujikawa, T., Ohashi, M., Maezawa, H., and Nakai, S. (1985) F-K XANES studies of alkaline-earth fluorides. Journal of the Physical Society of Japan, 54, 4027–4033.

Otten, M.T., and Buseck, P.R. (1987) The oxidation state of Ti in hornblende and biotite determined by electron energy loss spectroscopy, with inferences regarding the Ti substitution. Physics and Chemistry of Minerals, 14, 45–51.

Otten, M.T., Miner, B., Rask, J.H., and Buseck, P.R. (1985) The determination of Ti, Mn and Fe oxidation states in minerals by electron energy-loss spectroscopy. Ultramicroscopy, 18, 285–290.

Paterson, J.H., and Krivanek, O.J. (1990) ELNES of 3d transition-metal oxides. II. Variations with oxidation state and crystal structure. Ultramicroscopy, 32, 319–325.

Pratt, G.W.J., and Coehlo, R. (1959) Optical absorption of CoO and MnO above and below the Neel temperature. Physics Review, 116, 281–286.

Rao, C.N.R., Sarma, D.D., Vasudevan, S., and Hegde, M.S. (1979) Study of transition metal oxides by photoelectron spectroscopy. Proceedings of the Royal Society London, A367, 239–252.

Rask, J.H., Miner, B.A., and Buseck, P.R. (1987) Determination of manganese oxidation states in solids by electron energy-loss spectroscopy. Ultramicroscopy, 21, 321–326.

Rez, P., Weng, X., and Ma, H. (1991) The interpretation of near edge structure. Microscopy, Microanalysis, Microstructures, 2, 143–151.

Robertson, J. (1986) Amorphous carbon. Advances in Physics, 35, 317–374.

Robertson, J., and O'Rielly, E.P. (1987) Electronic and atomic structure of amorphous carbon. Physical Review, B35, 2946–2957.

Rosenberg, R.A., Love, P.J., and Rehn, V. (1986) Polarization-dependent C(*K*) near-edge x-ray-absorption fine structure of graphite. Physical Review B, 33, 4034–4037.

Rossman, G.R. (1988) Optical spectroscopy. Mineralogical Society of America Reviews in Mineralogy, 18, 207–254.

Sauer, H., Brydson, R., Rowley, P.N., Engel, W., and Thomas, J.M. (1993) Determination of coordinations and coordination-specific site occupancies by electron energy-loss spectroscopy: An investigation of boron-oxygen compounds. Ultramicroscopy, 49, 198–209.

Shinohara, H., Sato, H., Saito, Y., Tohji, K., Matsuoka, I., and Udagawa, Y. (1991) Carbon *K*-edge X-ray absorption near-edge structures of solid C_{70}. Chemical Physics Letters, 183, 145–148.

Sipr, O. (1992) Real-space multiple-scattering analysis of x-ray absorption near-edge *K* spectra of Cu_2O and CuO. Journal of Physics: Condensed Matter, 4, 9389–9400.

Taftø, J., and Zhu, J. (1982) ELNES, a potential technique in the studies of local atomic arrangements. Ultramicroscopy, 9, 349–354.

Terminello, L.J., Shuh, D.K., Himpsel, F.J., Lapiano-Smith, D.A., Stöhr, J., Bethune, D.S., and Meijer, G. (1991) Unfilled orbitals of C_{60} and C_{70} from carbon *K*-shell X-ray absorption fine structure. Chemical Physics Letters, 182, 491–496.

Thole, B.T., and van der Laan, G. (1988) Branching ratio in x-ray absorption spectroscopy. Physical Review, B38, 3158–3171.

Tyrna, P.L., and Guggenheim, S. (1991) The crystal structure of norrishite, $KLiMn_2^{3+}Si_4O_{12}$: An oxygen-rich mica. American Mineralogist, 76, 266–271.

van der Laan, G. (1991) $M_{2,3}$ absorption spectroscopy of 3d transition-metal compounds. Journal of Physics: Condensed Matter, 3, 7443–7454.

van der Laan, G., and Kirkman, I.W. (1992) The 2p absorption spectra of 3d transition metal compounds in tetrahedral and octahedral symmetry. Journal of Physics: Condensed Matter, 4, 4189–4204.

van der Laan, G., Zaanen, J., Sawatzky, G.A., Karnatak, R., and Esteva, J.-M. (1986) Comparison of x-ray absorption with x-ray photoemission of nickel dihalides and NiO. Physical Review, B33, 4253–4263.

van der Laan, G., Pattrick, R.A.D., Henderson, C.M.B., and Vaughan, D.J. (1992) Oxidation state variations in copper minerals studied with Cu 2P X-ray absorption spectroscopy. Journal of Physics and Chemistry of Solids, 53, 1185–1190.

van der Pluijm, B.A., Lee, J.H., and Peacor, D.R. (1988) Analytical electron microscopy and the problem of potassium diffusion. Clays and Clay Minerals, 36, 498–504.

Vvedensky, D.D., Saldin, D.K., and Pendry, J.B. (1986) An update of DLXANES, the calculation of X-ray absorption near-edge structure. Computer Physics Communications, 40, 421–440.

Walls, M.G., and Tencé, M.G. (1989) EELS study of beam-induced decomposition of calcite in the STEM. In P.J. Goodhew and H.Y. Elder, Eds., Proceedings of the Institute of Physics Electron Microscopy and Analysis Group and Royal Microscopical Society Conference, p. 255–258. Institute of Physics Conference Series no. 98, Institute of Physics, Bristol.

Weng, X., Rez, P., and Ma, H. (1989a) Carbon *K*-shell near-edge structure: Multiple scattering and band-theory calculations. Physical Review, B40, 4175–4178.

Weng, X., Rez, P., and Sankey, O.F. (1989b) Pseudo-atomic-orbital band theory applied to electron-energy-loss near-edge structures. Physical Review, B40, 5694–5704.

Weng, X., Rez, P., and Batson, P.E. (1990) Single electron calculations for the Si $L_{2,3}$ near edge structure. Solid State Communications, 74, 1013–1015.

Wood, P.R., and Urch, D.S. (1976) Valence-band X-ray emission spectra of manganese in various oxidation states. Journal of the Chemical Society, Dalton Transactions, Part 3, 2472–2476.

Yang, K., and Seccombe, P.K. (1993) Chemical variation of chromite in the ultramafic cumulates of the Great Serpentine Belt, Upper Bingara to Doonba, New South Wales, Australia. Canadian Mineralogist, 31, 75–87.

Manuscript received July 2, 1993
Manuscript accepted December 29, 1993